X-ray and Neutron Scattering and Solid State NMR Investigations on Precursor-Derived B–C–N Ceramics Using Isotopic Substitution

Dieter Sauter,*,[†] Markus Weinmann,[†] Frank Berger,[‡] Peter Lamparter,[†] Klaus Müller,[‡] and Fritz Aldinger[†]

Max-Planck-Institut für Metallforschung and Institut für Nichtmetallische Anorganische Materialien, Universität Stuttgart Pulvermetallurgisches Laboratorium, Heisenbergstrasse 5, D-70569 Stuttgart, Germany, and Institut für Physikalische Chemie, Universität Stuttgart, Pfaffenwaldring 55, D-70569 Stuttgart, Germany

Amorphous B–C–N ceramics were produced by thermolysis of poly(borosesquicarbodiimide) of idealized formula $[B_2(NCN)_3]_n$ at 1100 °C in an argon atmosphere. Their structure was investigated by X-ray and neutron diffraction. Wide-angle diffraction showed that the ceramics consist of an amorphous structure with hexagonal planar near-range ordered atomic arrangements similar to graphite. Additionally, magic-angle spinning nuclear magnetic resonance (MAS NMR) studies demonstrated that boron is preferentially trigonally bonded to nitrogen. Small-angle scattering (SAS) experiments revealed that the as-thermolyzed ceramics are inhomogeneous. By combined small-angle X-ray and neutron scattering experiments the medium-range order and its temperature dependency were investigated. Contrast variation studies using isotopic substitution (^{nat}N vs ^{15}N) suggest that the ceramics contains sub-microscopic pores. The Guinier radius (R_G) of the pores increases upon annealing. Positron annihilation investigations of the ceramics also revealed the presence of nanopores.

1. Introduction

Ternary B–C–N ceramics should possess remarkable properties because the constituting binary phases exhibit high thermal stability (h-BN), outstanding hardness (c-BN, B_4C), conducting properties (C), and chemical inertness. B–C–N materials therefore have become the topic of a large number of research papers since the early 1970s when the first reports on synthesis and investigation of ternary compounds appeared.[1,2] An extensive list of publications on this subject can be found in refs 3 and 4. A very promising way to control the evolution of material structure and properties is given by the thermolytic conversion of suitable organoelement polymers to multinary ceramics.[5] The synthesis of polymeric borosesquicarbodiimide and its ceramization (25–1100 °C) to a B–C–N material in an argon atmosphere is reported in ref 6.

Despite numerous reports on the synthesis of boron carbonitrides in a variety of chemical processes using different precursors, there is still a lack of evidence that all, or at least some, of the reported B–C–N ceramics are mechanical mixtures of turbostratically distorted graphite and hexagonal boron nitride rather than substitutional solid solutions of all three elements in a honeycomb network. Literature results on this topic[7–13] offer only a speculative knowledge on the nature of the various B–C–N ceramics. Challenges of the distinction between the two types of the atomic arrangement are yet to be fully resolved. Thus, additional theoretical and experimental work is needed.

The present study is an attempt to obtain further insight into the atomic arrangement of amorphous B–C–N ceramics, annealed at different temperatures.

2. Theoretical Background

In the following the essential definitions are briefly summarized. For a more detailed description we refer to the review, ref 14.

* To whom correspondence should be addressed.

[†] Max-Planck-Institut für Metallforschung Stuttgart.

[‡] Universität Stuttgart.

(1) Kosolapova, T. Y.; Makarenko, G. N.; Serebryakova, T. I. *É. Poroshk. Metall.* **1971**, *97* (1), 27–33.

(2) Badzian, A. R.; Niemyski, T.; Appenheimer, S.; Olkuśnik, E. Graphite-boron nitride solid solutions by chemical vapour deposition. In *Proc. 3rd. Int. Conf. Chem. Vap. Deposition, Salt Lake City, UT, April 24–27*; Glaski, F. A., Ed.; American Nuclear Society, Hinsdale, IL, 1972; pp 747–753.

(3) Polo, M. C.; Martinez, E.; Esteve, J.; Andujar, J. L. *Diamond Relat. Mater.* **1998**, *7,* 376.

(4) Kawaguchi, M.; Kawashima, T. *J. Chem. Soc., Chem. Commun.* **1993**, 1133–1134.

(5) Bill, J.; Aldinger, F. *Adv. Mater.* **1995**, *7* (9), 775–787.

(6) Aldinger, F.; Bill, J.; Wurm, K. Offenlegungsschrift DE 196 34 777 A1, 1998.

(7) Derre, A.; Filipozzi, L.; Peron, F. *J. Phys. IV, Suppl. C3* **1993**, *3,* 195.

(8) Derre, A.; Filipozzi, L.; Bouyer, F.; Marchand, A. *J. Mater. Sci.* **1994**, *29,* 1589.

(9) Andreev, Y. G.; Lundström, T.; Harris, R. K.; Oh, S.-W.; Apperley, D. C.; Thomson, D. P. *J. Alloys Compd.* **1995**, *227,* 102–108.

(10) Andreev, Y. G.; Lundström, T. *J. Alloys. Compd.* **1994**, *210,* 311.

(11) Kouvetakis, J.; Sasaki, T.; Shen, C.; Hagiwara, R.; Lerner, M.; Krishnan, K. M.; Bartlett, N. *Synth. Met.* **1989**, *34,* 1–7.

(12) Kaner, R. B.; Kouvetakis, J.; Warble, C. E.; Sattler, M. L.; Bartlett, N. *Mater. Res. Bull.* **1987**, *22,* 399–404.

(13) Bill, J.; Friess, M.; Riedel, R. *Eur. J. Solid State Inorg. Chem.* **1992**, *29* (5), 195–212.

2.1. Atomic Short-Range Order and Wide-Angle Scattering. From the scattering experiment, after application of the appropriate corrections, the total structure factor $S(q)$ according to Faber and Ziman[15] is obtained from the coherently scattered intensity per atom $I(q)$,

$$S(q) = \frac{I(q) - [\langle f(q)^2 \rangle - \langle f(q) \rangle^2]}{\langle f(q) \rangle^2} \quad (1)$$

where $q = |\vec{q}| = 4\pi(\sin\Theta)/\lambda$ is the wave vector transfer, 2Θ the scattering angle, and λ the wavelength. In this definition the Laue monotonic scattering $[\langle f(q)^2 \rangle - \langle f(q) \rangle^2]$ is subtracted. The brackets $\langle\ \rangle$ denote compositional averages of the scattering lengths f_i of the atomic species i, with atom fractions c_i. The relations between the structure factors and the pair correlation functions, for the total as well as the partial ones, is given by Fourier transformation. The total pair correlation function $G(r)$

$$G(r) = \frac{2}{\pi} \int_0^\infty q[S(q) - 1]\sin(qr)\,dq \quad (2)$$

is a weighted sum of the partial pair correlation functions $G_{ij}(r)$:

$$G(r) = \sum_{i=1}^n \sum_{j=1}^n \frac{c_i c_j f_i f_j}{\langle f \rangle^2} \cdot G_{ij}(r) \quad (3)$$

$$= \sum_{i=1}^n \sum_{j=1}^n W_{ij} \cdot G_{ij}(r) \quad (4)$$

In the case of a ternary system ($n = 3$), one needs six partial $G_{ij}(r)$ functions for the structural description of the system (note that $G_{ij}(r) = G_{ji}(r)$).

The corresponding partial radial distribution function $RDF_{ij}(r)$ can then be calculated as

$$RDF_{ij}(r) = 4\pi r^2 \rho_{ij}(r) \quad (5)$$

$$= c_j[rG_{ij}(r) + 4\pi r^2 \rho_0] \quad (6)$$

The partial pair density distribution function $\rho_{ij}(r)$ describes the number of j-type atoms per unit volume at distance r from an i-type atom at $r = 0$, where ρ_0 is the mean atomic number density.

The partial coordination numbers Z_{ij} are obtained from $\rho_{ij}(r)$ by integration over the maximum

$$Z_{ij} = \int_{r_x}^{r_y} 4\pi r^2 \rho_{ij}(r)\,dr \quad (7)$$

where r_x and r_y define the corresponding coordination shell.

2.2. Inhomogeneities and Small-Angle Scattering. If a sample is not homogeneous, but contains fluctuations of the composition and/or density on a medium-range scale beyond the scale of atomic distances, say beyond 5 Å, a small-angle scattering effect may be observed.[16-18] In the case of phase separation

that means the sample consists of regions p with a volume fraction c within a matrix m, from the coherently scattered intensity per volume, $I(q)$, several properties of these regions can be derived.

It is possible to determine the dimension of the scattering regions by the investigation of the Guinier range.[16] In the Guinier approximation at small q's the corrected and normalized coherently scattered intensity $I(q)$ is given by

$$I(q) = I(q=0) \cdot \exp\left(-\frac{R_G^2 \cdot q^2}{3}\right) \quad (8)$$

where R_G is the so-called Guinier radius. This radius R_G represents a first approximation of the dimension of the scattering regions. To calculate the size of the regions, it is necessary to know the shape of the regions.

Further information about the scattering objects can be derived from the integrated intensity Q, the so-called invariant,

$$Q \equiv \int_0^\infty I(q) \cdot q^2\,dq = 2\pi^2 \cdot c(1 - c) \cdot (\Delta\eta)^2 \quad (9)$$

where $\Delta\eta$ is the difference of the mean scattering length densities of region p and matrix m. Taking into account that the average scattering lengths $\langle b \rangle_p$ and $\langle b \rangle_m$ can be calculated from the composition and the atomic density of region ρ_{0p} and matrix ρ_{0m}, $\Delta\eta$ can be calculated as

$$\Delta\eta = \rho_{0p} \cdot \langle b \rangle_p - \rho_{0m} \cdot \langle b \rangle_m = \rho_{0p} \cdot \left(\sum_{i=0}^n c_i \cdot \eta_i\right)_p - \rho_{0m} \cdot$$

$$\left(\sum_{j=0}^n c_j \cdot \eta_j\right)_m \quad (10)$$

From the intensity at zero scattering angle $I(q=0)$,

$$I(q=0) = \overline{\delta\eta^2} \cdot V_c = c \cdot (1 - c) \cdot (\Delta\eta)^2 \cdot V_c \quad (11)$$

the correlation volume V_c can be determined. It is defined as

$$V_c \equiv \int_0^\infty 4\pi r^2 \cdot \gamma_0(r)\,dr \quad (12)$$

where $\gamma_0(r)$ is the autocorrelation function of the scattering density fluctuations in the system. Using the contrast variation between neutron and X-ray diffraction and between diffent isotopes in neutron scattering, information about the scattering objects can be derived. For example, combining X-ray[(x)] and neutron[(n)] scattering, the relation

$$\frac{(\Delta^x\eta^2)}{(\Delta^n\eta^2)} = \frac{{}^xQ}{{}^nQ} = \frac{{}^xI(q=0)}{{}^nI(q=0)} \quad (13)$$

yields a characteristic value for a certain type of region within a matrix if the two samples have the same

(14) Lamparter, P.; Steeb, S. Structure of Amorphous and Molten Alloys. In *Materials Science and Technology*; VCH: New York, 1993; Vol. 1, pp 217−288.
(15) Faber, T. E.; Ziman, J. M. *Philos. Mag.* **1965**, *11*, 153.

(16) Guinier, A.; Fournet, G. *Small Angle Scattering of X-rays*; John Wiley and Sons Inc.: New York, 1955.
(17) Feigin, L. A.; Servgun, D. I. *Structure Analysis by Small Angle X-ray and Neutron Scattering*; Plenum Press: New York, 1987.
(18) Glatter, O.; Kratky, O. *Small-Angle X-ray Scattering*; Academic Press Inc.: London, 1982.

chemical composition. For a supposed type of region the left side of eq 13 can be calculated (eq 10) and the right side of the relation can be determined from the experiments. The agreement of the two values provides a criterion to establish the chemical composition of the scattering objects *p*.

2.3. Nuclear Magnetic Resonance (NMR) Theory. In the following we briefly review some points which are important for the understanding of quadrupolar NMR line shapes. Further details can be found for example in ref 19. In general, such NMR line shapes are dominated by the quadrupolar interaction arising from the interaction between the nuclear quadrupolar moment and the electric field gradient. In many cases rather large values for the quadrupolar coupling constant (QCC) with values in the MHz range are observed. The quadrupolar interaction thus gives rise to both first- and second-order corrections to the Zeeman energy levels.

In the case of central transition (CT) spectra ($m = (^1/_2 \rightarrow -^1/_2$ transition) the overall line shape is solely determined by the second-order contribution of the quadrupolar interaction.[20] As a result, very characteristic CT NMR line shapes are found if powder samples are considered. Here, the angular dependence of the quadrupolar interaction contains both second-order P_2-(cos Θ) and fourth-order P_4(cos Θ) Legendre terms. For this reason fast rotation of the sample at the magic angle cannot remove the second-order quadrupolar contribution completely. Again, in the case of fast magic-angle spinning, one is left with a characteristic powder pattern; the width of the spectrum however is reduced to some extent. With the assumption that the asymmetry parameter η is taken to 0, the CT MAS spectrum shows two singularities at positions ν_1 and ν_2 as well as a shoulder at position ν_3 (compare experimental ^{11}B NMR spectra in Figure 4). Their positions are given by[19]

$$\nu_1 - \nu_L = \frac{-4}{21} \cdot A; \quad \nu_2 - \nu_L = \frac{-15}{18} \cdot A; \quad \nu_3 - \nu_L = \frac{-12}{9} \cdot A \quad (14)$$

with

$$A = \frac{\nu_Q^2}{\nu_L}\left[I(I+1) - \frac{3}{4}\right]; \quad \nu_Q = \frac{3e^2qQ}{2I(2I-1)h} \quad (15)$$

ν_L is the Larmor frequency and the quadrupolar coupling constant (QCC) is given by the quantity e^2qQ/h.

At the same time, a shift of the center of gravity in the CT NMR line shape is observed. For an $I = ^3/_2$ nucleus the shift δ_{QS} is given by[21]

$$\delta_{QS} = -\frac{1}{40} \cdot \frac{C_Q^2}{\nu_L^2} \quad (16)$$

Satellite transition (SATRAS) spectra (e.g., $m = ^3/_2 \rightarrow ^1/_2$ and $-^1/_2 \rightarrow -^3/_2$ transitions for an $I = ^3/_2$ nucleus such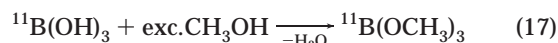 as [11]B) only reflect first-order quadrupolar effects and thus are determined by second-order P_2(cos Θ) terms. In principle, magic-angle sample spinning therefore is applicable to the removal of quadrupolar effects in SATRAS spectra. Usually, the QCC, however, is far too large as compared to the sample rotation frequency. For the satellite transitions thus a series of narrow rotational sidebands occurs symmetrically around the CT, covering a wide range of frequencies.[21,22] The overall shape of the SATRAS spectrum monitors the static line shape of the satellite transition, which is determined by the QCC and the asymmetry parameter η. To detect SATRAS spectra, very short pulses ($\cong$0.6 μs) and high spinning speeds ($\geq$10 kHz) are required.

3. Experimental Section

3.1. Sample Preparation. B−C−N ceramics were produced by thermolysis of poly(borosesquicarbodiimide),[6] which itself was synthesized by the reaction of cyanamide with triethylaminborane in tetrahydofuran (THF) solution in an argon atmosphere using the standard techniques developed by Wilhelm Schlenk. All apparatus are equipped with sidearms for the evacuation and introduction of inert gas.[23] Because of the high neutron absorption cross section of natural boron, $\sigma_{atom} = 767 \times 10^{-24}cm^2$, it was necessary to prepare [11]B ($\sigma_{atom} = 0.006 \times 10^{-24}$ cm^2) labeled samples. Because the different carbon isotopes exhibit no significant differences in their coherent scattering lengths, the only feasible contrast variation in neutron scattering is the isotopic substitution of natural nitrogen ($b_{atom}^{natN} = 0.93 \times 10^{-12}cm$) by the isotope [15]N ($b_{atom}^{15N} = 0.64 \times 10^{-12}cm$). Therefore, for the neutron scattering experiments, samples were prepared containing nitrogen with natural isotopic abundances as well as ^{15}N-enriched samples.

3.1.1. Synthesis of Triethylamine[11]Borane, [11]BH$_3$ × N(C$_2$H$_5$)$_3$. Because the starting compound triethylamine [11]Borane, [11]BH$_3$ × N(C$_2$H$_5$)$_3$, is not commercially available, it was synthesized in a two-step reaction starting from [11]Boron acid, [11]B(OH)$_3$ via [11]B-trimethylborate, [11]B(OCH$_3$)$_3$.[24]

(1) Synthesis of [11]B-trimethylborate, [11]B(OCH$_3$)$_3$[25]

$$^{11}B(OH)_3 + exc.CH_3OH \xrightarrow[-H_2O]{} {}^{11}B(OCH_3)_3 \quad (17)$$

[11]B(OH)$_3$ (50 g, 800 mmol) and 700 mL of methanol are mixed and refluxed for 1 h. When the boron acid is completely dissolved, the mixture is cooled to room temperature. Then, 120 g (870 mmol) of magnesium sulfate monohydrate MgSO$_4$ × H$_2$O, beforehand dried at 130 °C for several hours, is added and the mixture is filtrated through a pad of Celite. The colorless filtrate is then distilled via a 40-cm Vigreux column whereby the oil bath temperature may not exeed 80 °C. The distillate contains [11]B(OH)$_3$/CH$_3$OH azeotrope, bp 50−60 °C, and methanol. After the mixture was cooled to 0 °C, 10 mass % of lithium chloride (beforehand dried for 5 days at 100 °C in high vacuum) is added carefully. The lower LiCl/methanol phase is refused and the upper phase, which contains the product, is purified by distillation at 60−64 °C to deliver 69% of [11]B(OH)$_3$.

(19) Freude, D.; Haase, J. *NMR Basic Principles and Progress*; Springer-Verlag: Berlin, 1993; Vol. 29, p 1.
(20) Kundla, E.; Samoson, A.; Lipmaa, E. *Chem. Phys. Lett.* **1981**, *83*, 229.
(21) Samoson, A. *Chem. Phys. Lett.* **1985**, *119*, 29.

(22) Jäger, C. *NMR Basic Principles and Progress*; Springer-Verlag: Berlin, 1994; Vol. 31.
(23) Shriver, D. F.; Drezdzon, M. A. *The Manipulation of Air-Sensitive Compounds,* 2nd ed.; Wiley: New York, 1986.
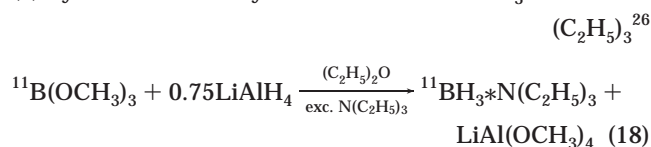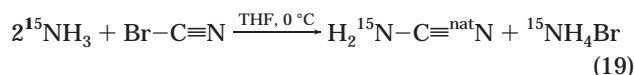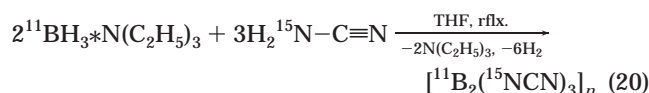(24) Nöth, H. Personal communication, 1999.
(25) Schlesinger, H. I.; Brown, H. C.; Mayerfield, D. L.; Gilbreath, J. R. *J. Am. Chem. Soc.* **1953**, *75* (1), 213−215.

(2) Synthesis of triethylamine ^{11}Borane, ^{11}BH$_3$*N(C$_2$H$_5$)$_3$[26]

$$^{11}B(OCH_3)_3 + 0.75 LiAlH_4 \xrightarrow[\text{exc. N(C_2H_5)_3}]{(C_2H_5)_2O} {}^{11}BH_3*N(C_2H_5)_3 + LiAl(OCH_3)_4 \quad (18)$$

Lithium aluminum hydride, LiAlH$_4$ (5.7 g, 150 mmol), is suspended in 100 mL of diethyl ether and then cooled at 0 °C; it is slowly added to 21 g (200 mmol) of ^{11}B-trimethylborate, ^{11}B(OCH$_3$)$_3$, dissolved in 80 mL of triethylamine, N(C$_2$H$_5$)$_3$. After the reaction is finished, the white precipitate that formed (LiAl(OCH$_3$)$_4$) is removed from the reaction mixture by filtration through Celite. The solvent is removed from the filtrate by vacuum evaporation at 40 °C/15 mm and the residue purified by distillation at 99–102 °C/15 mm to deliver ^{11}BH$_3$*N(C$_2$H$_5$)$_3$ in 54% yield.

3.1.2. Synthesis of ^{15}N-Cyanamide, H$_2$^{15}N−C≡N.

$$2^{15}NH_3 + Br-C\equiv N \xrightarrow{\text{THF, 0 °C}} H_2{}^{15}N-C\equiv{}^{nat}N + {}^{15}NH_4Br \quad (19)$$

Bromocyan, Br−C≡N (53 g, 500 mmol), is dissolved in 1000 mL of tetrahydrofuran and cooled to 0 °C. Under vigorous stirring, 18 g (1000 mmol) of ^{15}N-ammonia, ^{15}NH$_3$, are slowly introduced, whereby the reaction mixture immediately becomes cloudy. The mixture is subsequently warmed to 25 °C and filtrated through a pad of Celite. The solvent is removed from the filtrate by vacuum evaporation and the white residue re-crystallized at −30 °C from 100 mL of *n*-pentane/tetrahydrofuran to deliver 20 g (465 mmol, 93%) of ^{15}N-cyanamide.

3.1.3. Synthesis of Poly(borosesquicarbodiimide), [B$_2$-(^{15}N=C=N)$_3$]$_n$.

$$2^{11}BH_3*N(C_2H_5)_3 + 3H_2{}^{15}N-C\equiv N \xrightarrow[-2N(C_2H_5)_3, -6H_2]{\text{THF, rflx.}} [{}^{11}B_2({}^{15}NCN)_3]_n \quad (20)$$

^{15}N-cyanamide (4.3 g, 100 mmol) and 7.7 g (67 mmol) of triethylamine ^{11}Borane are dissolved in 300 mL of tetrahydrofuran. The mixture is refluxed for 48 h. Under moderate gas evolution it clouds because of the precipitation of the product. After removal of the volatile part in high vacuum at a maximum of 60 °C, 4.8 g (33 mmol) of [B$_2$(^{15}N=C=N)$_3$]$_n$ are obtained as a colorless solid that is very sensitive to oxygen and moisture.

3.2. Sample Treatment. To avoid oxygen contamination, both polymers (one containing the isotope ^{15}N and the other containing ^{nat}N) were directly thermolyzed at 1100 °C in an argon atmosphere without further processing steps. Hence, the heat treatment yielded spongelike black solids of amorphous B−C−N. After thermolysis, parts of the samples were additionally annealed in a nitrogen atmosphere for 16 h at 1200, 1400, 1600, 1700, 1850, and 2000 °C, respectively. Annealing of the ceramics at temperatures up to 1700 °C yielded almost the same composition. During annealing at temperatures higher than 1700 °C, the samples decomposed predominantly to products of carbon. In each case the samples were crushed into coarse powders. The chemical compositions of the ceramic materials and their atomic densities, ρ_0, are shown in Table 1. The atomic densities were determined by using a helium pygnometer. The oxygen contamination was determined by using chemical analysis. It was neglected in the analysis of the scattering data. The hydrogen content in the materials was below the sensitivity of chemical analysis, but could be estimated from neutron wide angle scattering to be smaller than 2 at. % at 1100 °C, decreasing with increasing annealing temperature.

Table 1. Chemical Compositions (at. %) (Error ±0.5), and Atomic Densities, ρ_0 (Error ±0.005)

sample	heat treatment	c_B	c_C	c_N	c_O	ρ_0 (Å^{-3})
^{11}B−C−N	1100 °C	32	37	23	8	0.102
^{11}B−C−N	1200 °C	29	37	28	6	0.102
^{11}B−C−N	1400 °C	33	34	31	2	0.104
^{11}B−C−N	1600 °C	31	36	31	2	0.104
^{11}B−C−N	1700 °C	31	36	31	2	0.105
^{11}B−C−N	1850 °C	6	88	6	-	0.052
^{11}B−C−N	2000 °C	7	87	6	-	0.059
^{11}B−C−^{nat,15}N	1200 °C	24	41	24	11	0.103
^{11}B−C−^{nat,15}N	1600 °C	28	43	27	2	0.103

3.3. Scattering Experiments. The X-ray wide-angle scattering measurements on the B−C−N ceramics were performed at the beamline ID01 of the ESRF (European Synchrotron Radiation Facility), Grenoble, France.[27] With use of synchrotron radiation of wavelength $\lambda = 0.62$ Å ($E = 19.99$ keV), the samples were investigated in transmission mode with very good counting statistics.[28] From the scattered intensities, recorded up to $q = 19$ Å^{-1}, after several corrections concerning the instrument and the measurement geometry, the structure factor $S(q)$ was derived according to eq 15.

The neutron scattering experiments were performed at the ISIS facility of the Rutherford Appleton Laboratory, Chilton, U.K., using the SANDALS instrument. The samples were placed in containers of vanadium. The intensities, measured up to $q = 50$ Å^{-1}, were corrected for background, absorption, multiple scattering, and incoherent scattering and normalized to $S(q)$ as described in ref 29.

The SAXS measurements were performed with Cu Kα radiation in pinhole collimation.[30] The B−C−N powders were encapsulated in containers with capton windows. For the neutron diffraction measurements the B−C−N powders were encapsulated in quartz glass. Small-angle neutron scattering (SANS) experiments were carried out at the Laboratoire Léon Brillouin (LLB) facility, CEA, Saclay, using the instrument PAXE with wavelengths between 4.5 and 15 Å.[31] Additionally, measurements with wavelengths of 5.1 Å were performed at the BENSC facility of HMI, Berlin, using the instrument V4.[32] The measured intensities were corrected for transmission, the instrumental background, and the contribution of the container and subsequently normalized to absolute scattering units.[33]

3.4. NMR Experiments. All NMR experiments were carried out on a Bruker MSL 300 spectrometer operating at a static magnetic field of 7.05 T (^{1}H frequency: 300.13 MHz) using a 4-mm magic-angle spinning (MAS) probe. ^{13}C, ^{15}N, and ^{11}B NMR experiments were done at 75.47, 30.42, and 96.26 MHz, respectively.

^{13}C and ^{15}N NMR spectra were recorded under MAS conditions (sample rotation frequency: 5 kHz) with either single-pulse (^{13}C, ^{15}N) or cross-polarization (CP) excitation (^{13}C), using $\pi/2$ pulse widths of 4.0 μs (^{13}C) and 7.5 μs (^{15}N). Recycle delays up to 40 s (^{15}N) and 120 s (^{13}C) were used during single-pulse excitation experiments. During the ^{13}C CP/MAS experiments spin lock fields of 62.5 kHz and contact times of 3 ms were employed at a recycle delay of 8 s. ^{13}C chemical shifts were determind relative to the external standard ada-

(26) Ruff, J. K.; Hawthorne, M. F. *J. Am. Chem. Soc.* **1960**, *82* (5), 2141–2144.

(27) Barrett, R.; Baruchel, J.; Haertwig, J.; Zontone, F. *J. Phys. D: Appl. Phys.* **1995**, *28*, A250−A255.

(28) Lequien, S.; Goirand, L.; Lesimple, F. *Rev. Sci. Instrum.* **1995**, *66*, 1725−1727.

(29) Soper, A. K.; Howells, W. S.; Hannon, A. C. *ATLAS Manual*; Neutron Science Division, Rutherford Appleton Laboratory; Chilton, OX11 0QX, United Kingdom, 1989.

(30) Härle, J. *Untersuchung schnell abgeschreckter Schnellarbeitstähle im Bereich groser und kleiner Impulsüberträge mittels Röntgenstrahlen*, Ph.D. Thesis, Universität Stuttgart, 1990.

(31) Kahn, R. *Equipements Experimentaux*; Laboratoire Léon Brillouin, Paris, France, Jan 1995.

(32) *Neutron-Scattering Instrumentation at the Research Reactor Ber II*; Berlin Neutron Scattering Center BENSC: Berlin, May 1996.

(33) Keiderling, U.; Wiedenmann, A. *Physica B* **1995**, *213/214*, 895−897.

Figure 1. Total structure factors $S(q)$ from neutron diffraction for heat-treated ^{11}B-substituted B−C−N ceramics.

Figure 2. Total neutron pair correlation functions $G(r)$. At small r the function $-4\pi r\rho_0$ is drawn for $\rho_0 = 0.102$ (cf. Table 1).

mantane. These values were then expressed relative to the reference compound tetramethylsilane (TMS) ($\delta = 0$ ppm). ^{15}N chemical shifts are given relative to CH$_3$NO$_2$ ($\delta = 0$ ppm) after external calibration with ^{15}NH$_4$^{15}NO$_3$ (NH$_4^+$: -358.4 ppm).

^{11}B NMR (central transition spectra) and ^{11}B SATRAS (satellite transition) spectra were recorded with single-pulse excitation using $\pi/3$ (pulse length: 2.4 μs) and $\pi/12$ (pulse length: 0.6 μs) pulses, respectively, and recycle delays of 2 s and a sample rotation frequency of 12 kHz. The spectra were calibrated relative to an aqueous solution of H$_3$BO$_3$ ($\delta = 19.6$ ppm) as external standard and are given relative to BF$_3$·OEt$_2$ ($\delta = 0$ ppm).

4. Results and Discussion

4.1. Atomic Structure. 4.1.1. Wide-Angle Scattering. The weighting factors W_{ij} of the partial G_{ij} according to eq 4 are almost the same for X-rays and neutrons, for the 1600 °C annealed sample, for example,

$$G(r)_{\text{X-ray}} = 0.065 \cdot G_{\text{BB}} + 0.188 \cdot G_{\text{BC}} + \\ 0.190 \cdot G_{\text{BN}} + 0.138 \cdot G_{\text{CC}} + 0.278 \cdot G_{\text{CN}} + \\ 0.141 \cdot G_{\text{NN}} \quad (21)$$

$$G(r)_{\text{neutron}} = 0.079 \cdot G_{\text{BB}} + 0.184 \cdot G_{\text{BC}} + \\ 0.219 \cdot G_{\text{BN}} + 0.108 \cdot G_{\text{CC}} + 0.257 \cdot G_{\text{CN}} + \\ 0.153 \cdot G_{\text{NN}} \quad (22)$$

where the $W_{ij}(q)$ for X-rays were averaged over $0 < q < 20$. Consequently, X-ray and neutron wide-angle scattering yields almost the same graph of the pair correlation functions and the contrast variation is not applicable for wide-angle scattering. Because of the extended range of q with neutron scattering, which is essential for the resolution of the individual atomic pairs $i - j$ in r space, only the results from the neutron scattering investigations are considered in the following.

In Figure 1 the total structure factors, $S(q)$, from neutron scattering are shown for ^{11}B-substituted B−C−N samples heat-treated at different temperatures. Between 1100 and 1400 °C the structure factor curves do not show distinct changes. The sample, annealed at 1600 °C, however, exhibits new peaks (arrows in Figure 1), which correspond to the 002 and 004 reflections in graphite and h-BN and which indicate the onset of crystallization.

The total pair correlation functions $G(r)$, obtained by Fourier transformation of the structure factors $S(q)$ from
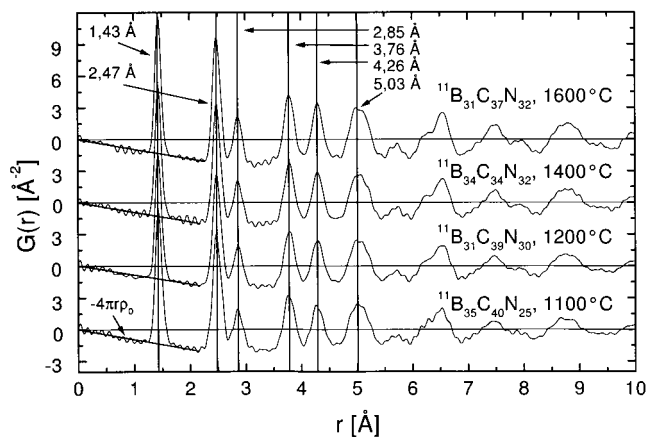
Figure 1, are shown in Figure 2. The ripples at small r values are caused by termination effects. Because of the covalent type of bonding, the structure of the amorphous phase consists of ordering within a range of several atomic distances ($r < 10$ Å). It is evident that for different annealing temperatures the total pair correlation functions are more or less identical. With neutrons up to $r < 5.5$ Å, six distinct peaks at 1.43, 2.47, 2.85, 3.76, 4.26, and 5.03 Å can be observed.

A comparison of observed peak positions with distances for relevant crystalline phases is given in Table 2. The peaks at 1.43, 2.47, and 2.85 Å are in agreement with C−C and B−N distances in graphite and hexagonal boron nitride, respectively, and are distinctly smaller than the corresponding ones in diamond. Distances corresponding to the B−C and C−N phases listed in Table 2 do not occur in the experimental $G(r)$ functions.

The apparent coordination number of the first three coordination shells (i.e., the peak areas A_x) was determined by fitting Gaussians to the corresponding total radial distribution functions RDF(r) as shown in Figure 3 and are listed in Table 3. Gaussian fitting to the RDF-(r), instead of $T(r) = G(r) + 4\pi r\rho_0$, was chosen because the peaks of the RDF(r) are quite symmetrical (cf. Figure 3). The atomic distances and the coordination numbers indicate that the short-range ordering in amorphous B−C−N ceramics consists of a honeycomb network (graphite-like structure).

Concerning the distribution of the different species, two extreme cases can be conceived: statistically distributed B, C, and N atoms in the honeycomb network or heterogeneous states, namely, consisting of amorphous carbon and amorphous boron nitride honeycombs. Note that for both cases the same peak positions in the $G(r)$ functions are expected, that is, very similar atomic distances of the different atomic pairs. Thus, the peak positions do not provide a criteria for the two cases.
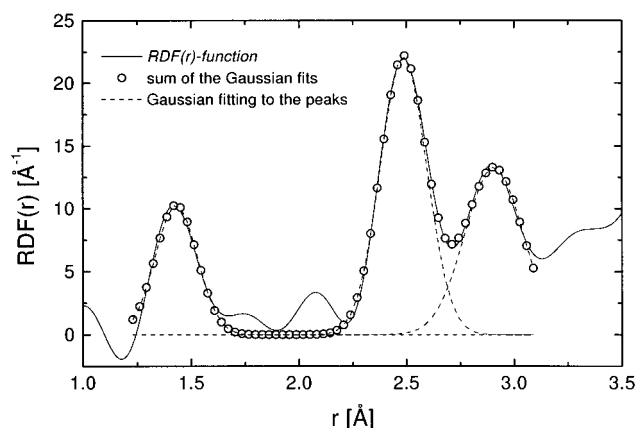
For both cases the expected areas of the first two peaks ($x = 1, 2$) can be calculated from

$$A_x = \sum_i \sum_j Z_{ij} \cdot \frac{W_{ij}}{c_j} \quad (23)$$

The partial pair coordination numbers Z_{ij} are known for both cases (e.g., for the statistical case: $Z_{ij} = c_j \cdot Z$,

Table 2. Atomic Distances for Amorphous $^{11}B_{31}-C_{39}-^{nat}N_{30}$ Annealed at 1200 °C (Error ± 0.2 Å) and for Relevant Crystalline Phases; Coordination Numbers Z_{ij} in Parentheses
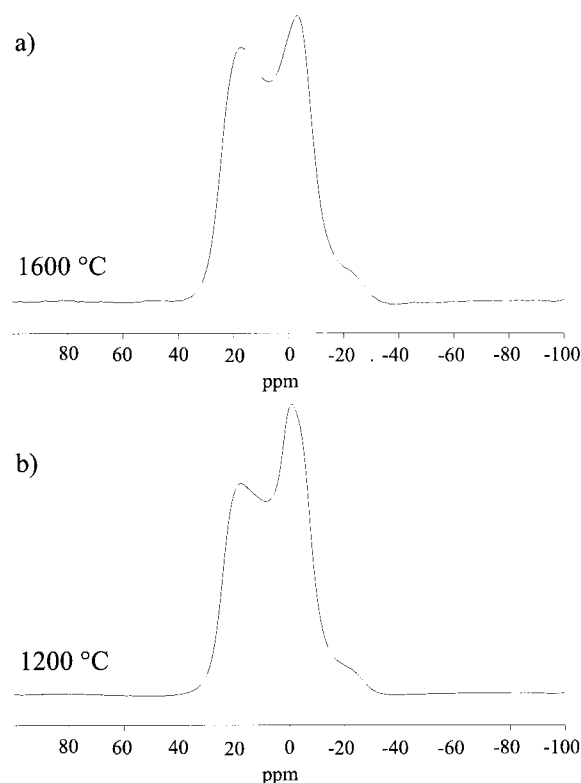
material	refs	distances r_{ij} (Å)							
		C–C	B–N	C–N	B–C	C–C	N–N	C–C	B–N
^{11}B–C–N		1.43				2.47		2.85	
diamond	50, 51	1.54 (4)				2.52 (12)		2.96 (12)	
α-graphite	52–54	1.42 (3)				2.46 (6)		2.84 (3)	
h-BN	55, 56		1.45 (3)				2.51 (6)		2.89 (3)
c-BN	56, 51		1.57 (4)				2.56 (12)		3.94 (12)
B$_4$C	51				1.72 (3.2)				
B$_4$C$_3$	51				1.67 (3.43)				
BC$_3$	57	1.42 (3)			1.55 (3)				
β-C$_3$N$_4$	58, 51			1.47 (3.43)			2.46, 2.69		

Figure 3. Amorphous $^{11}B_{31}C_{39}{}^{nat}N_{30}$, 1200 °C; Gaussian fitting to the peaks at 1.43, 2.47, and 2.85 Å of the RDF(r) function corresponding to the $G_n(r)$ from Figure 2.

Table 3. Peak Areas, A_x (Error ± 0.1), Determined from Gaussian Fits to the Total RDF(r) from Neutron Scattering (cf. Figure 3)

peak position $r_{ij} \pm 0.02$ (Å):	-	1.43	2.47	2.85
sample			peak area A_x	
$^{11}B_{35}C_{40}{}^{nat}N_{25}$, 1100 °C		3.0	6.0	4.2
$^{11}B_{31}C_{39}{}^{nat}N_{30}$, 1200 °C		2.8	6.1	4.0
$^{11}B_{34}C_{34}{}^{nat}N_{32}$, 1400 °C		2.7	5.8	4.8
$^{11}B_{31}C_{37}{}^{nat}N_{32}$, 1600 °C		2.8	6.1	4.5

where $Z = 3$ or 6, respectively; for the phase-separated case: $Z_{CB} = Z_{CN} = Z_{BB} = Z_{NN} = 0$, $Z_{BN} = 3$ (first shell)). However, it turned out that for both cases almost the same result was obtained, $A_1 \approx 3$ and $A_2 \approx 6$ for the first and second shell. This is explained by the rather small scattering contrast between the different atomic species. This means that using wide-angle scattering it is not possible for distinguishing between a statistical distribution of all three species or a separation of BN and C (see, however, the NMR results in the following section).

4.1.2. NMR Experiments. Multinuclear NMR studies were performed to obtain further insight into the local order of amorphous B–C–N ceramics.[34-36] In Figure 4 representative ^{11}B NMR spectra are given for the sample without ^{15}N enrichment. The spectra of the ^{15}N-enriched samples were found to be identical. The characteristic ^{11}B NMR line shape observed for the

(34) Schmidt-Rohr, K.; Spiess, H. W. *Multidimensional Solid-State NMR and Polymers*; Academic Press: London, 1994.
(35) Mehring, M. *Principles of High-Resolution NMR in Solids*; Springer-Verlag: Berlin, 1983.
(36) Haeberlen, U. *High-Resolution NMR in Solids*; Academic Press: New York, 1976.

Figure 4. ^{11}BNMR spectra for the amorphous ^{11}B–C–N ceramic annealed at (a) 1600 °C and (b) 1200 °C. NMR measurements were done at room temperature; indicated temperatures refer to annealing temperatures of the samples.

sample, annealed at 1600 °C, can be explained by the presence of a second-order quadrupolar broadening arising from a strong quadrupolar interaction and which cannot be removed by magic-angle sample spinning (see Theoretical Background section). Generally, the quadrupolar coupling constant strongly depends on the actual coordination. That is, trigonally coordinated ^{11}B nuclei (BX$_3$ sites) possess large quadrupolar coupling constants, while small quadrupolar coupling constants are found for tetrahedral coordination (BX$_4$ sites). Analysis of the ^{11}B NMR spectra clearly demonstrates that the spectrum is dominated by a spectral component due to trigonally coordinated boron nuclei with a quadrupolar coupling constant of QCC = 2.9 MHz and an asymmetry parameter of $\eta = 0$, which is in good agreement with the results of Marchetti et al.[37] for trigonally coordinated boron in h-BN. In addition, a small fraction of tetragonally coordinated boron nuclei

(37) Marchetti, P. S.; Kwon, D.; Schmidt, W. R.; Interrante, L. V.; Maciel, G. E. *Chem. Mater.* **1991**, *3*, 482–486.
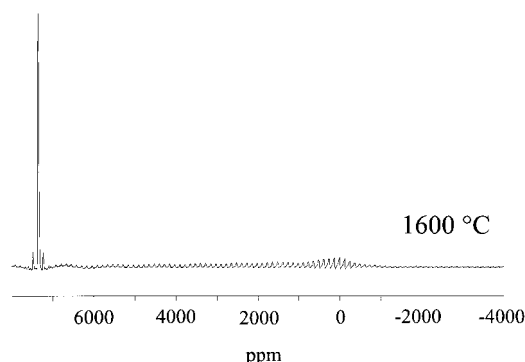
Figure 5. ^{11}B SATRAS NMR spectrum of the amorphous [11]B−C−N ceramic annealed at 1600 °C. Only the high field part of the spectrum is shown. NMR measurements were done at room temperature; indicated temperatures refer to annealing temperatures of the samples.

is present, which gives rise to an isotropic spectral component at 0 ppm. The presence of mainly trigonally coordinated boron, that is, planar BN_3 units, is further supported by the [11]B satellite transition (SATRAS) NMR spectrum,[21,38] given in Figure 5. Such SATRAS spectra are dominated by first-order quadrupolar coupling effects, where the spectral widths are directly proportional to the size of the quadrupolar coupling constants.[19] In the present case the width of the spinning sideband pattern is found to be spread over about 7000 ppm, with an overall shape being very close to that reported for h-BN.[39−41]

A lower annealing temperature of 1200 °C does not change the general picture of the (local) molecular structure. Here, the relative amount of trigonally coordinated boron nuclei (isotropic resonance at 0 ppm) is slightly enhanced (amount ≈10%). The ^{11}B NMR spectrum, however, is still dominated by trigonally coordinated boron nuclei which display the same magnetic parameters (QCC, η, and chemical shift) as discussed for the sample at 1600 °C. From these ^{11}B NMR data it is very unlikely that B−C bonds exist in the samples examined here. According to earlier ^{11}B solution NMR studies, the replacement of a B−N bond by a B−C bond should give rise to a downfield shift of the [11]B resonance. The [11]B isotropic chemical shifts of BN_3, BN_2C, and BC_3 sites thus typically range from 25 to 30 ppm, 30 to 35 ppm, and 65 to 85 ppm, respectively.[42] The [11]B isotropic chemical shift value of 30 ppm found for the present B−C−N sample again fits with the value reported for hexagonal BN, that is, BN_3 sites.[37]

^{15}N NMR spectra of the ^{15}N enriched sample, referring to the same annealing temperatures of 1200 and 1600 °C, are shown in Figure 6. At 1600 °C a single resonance located at $\delta(^{15}N) = -280$ ppm is visible. At 1200 °C this signal is accompanied by spinning sidebands (indicated by asterisks) as well as a smaller peak at −357 ppm. The low field resonance at −280 ppm
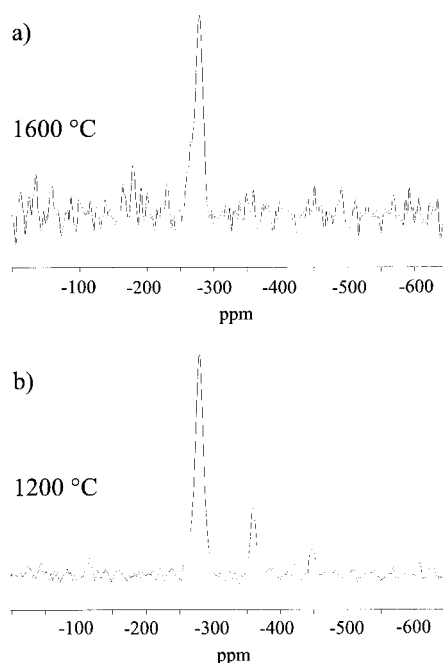

Figure 6. ^{15}N NMR spectra of the amorphous [11]B−C−[15,nat]N ceramic annealed at (a) 1600 °C and (b) 1200 °C. NMR measurements were done at room temperature; indicated temperatures refer to annealing temperatures of the samples.

clearly proves the presence of trigonally coordinated nitrogen atoms.[43] In fact, for h-BN a value of $\delta(^{15}N) = -285$ ppm has been reported.[44,45] The high field peak at −357 ppm again can be attributed to the presence of a small amount of tetragonally coordinated nitrogen nuclei (NB_4 sites), being consistent with the above results from the ^{11}B NMR data.[43]

Finally, in Figure 7 ^{13}C NMR spectra of the sample, annealed at 1200 °C, are given, which were recorded with (a) single-pulse and (b) cross-polarization excitation. In both cases a broad resonance centered at about 130 ppm is visible, which can be assigned to amorphous (graphite-like) carbon. Obviously, even at such high annealing temperatures, a finite amount of protons is present in the sample, which is a result of the preparation process. ^{1}H NMR experiments have therefore been performed, which in fact revealed a broad (unstructured) ^{1}H spectrum at this annealing temperature. This is agreement with other studies on precursor-derived ceramics where protons also could be observed well beyond 1000 °C.[41,46] It should be noted that ^{13}C NMR experiments were also conducted for the sample, annealed at 1600 °C, under both single-pulse and cross-polarization conditions. However, so far ^{13}C NMR signals could not be detected in this case, although recycle delays up to 12 min were employed. Most probably, the ^{13}C spin lattice relaxation time for this sample becomes too long because of the lack of efficient relaxation pathways.

(38) Skibsted, J.; Nielsen, N. C.; Bildsoe, H.; Jakobsen, H. J. *J. Magn. Reson.* **1991**, *95*, 88.
(39) Schuhmacher, J.; Müller, K. *Werkstoffwoche 98-Band VII: Symposium 9: Keramik*; Wiley-VCH: New York, 1998; p 321.
(40) van Wüllen, L.; Müller-Warmuth, W. *Solid State Nucl. Magn. Reson.* **1993**, *2*, 279−284.
(41) Schuhmacher, J.; Berger, F.; Weinmann, M.; Bill, J.; Aldinger, F.; Müller, K. *Appl. Organomet. Chem.* **2000**, *15*, 809.
(42) Nöth, H.; Wrackmeyer, B. *NMR Basic Principles and Progress*; Springer-Verlag: Berlin, 1978; Vol. 14, p 1.

(43) Gervais, C.; Babonneau, F.; Maquet, J.; Bonhomme, C.; Massiot, D.; Framery, E.; Vaultier, M. *Magn. Reson. Chem.* **1998**, *36*, 407−414.
(44) Gastreich, C. M. M. M. *J. Comput. Chem* **1998**, *19*, 711.
(45) Jeschke, G.; Hoffbauer, W.; Jansen, M. *Solid State Nucl. Magn. Reson.* **1998**, *12*, 1.
(46) Schuhmacher, J.; Weinmann, M.; Bill, J.; Aldinger, F.; Müller, K. *Chem. Mater.* **1998**, *10*, 3913.
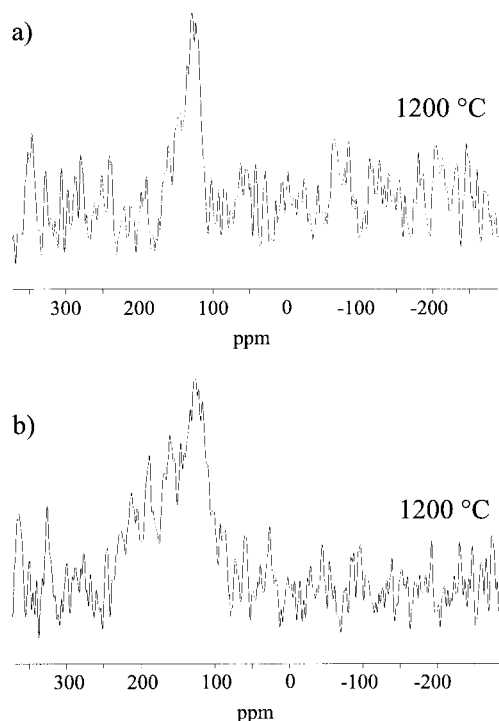
a)

1200 °C

| | | | | | |
|300|200|100|0|-100|-200|

ppm

b)

1200 °C

| | | | | | |
|300|200|100|0|-100|-200|

ppm

Figure 7. ^{13}C NMR spectra for the amorphous ^{11}B−C−N ceramic annealed at 1200 °C: (a) single-pulse and (b) cross-polarization excitation. NMR measurements were done at room temperature; indicated temperatures refer to annealing temperatures of the samples.

Table 4. Guinier Radii R_G of Amorphous ^{11}B−C−^{nat}N Ceramics Annealed at Different Temperatures from Neutron and X-ray Scattering; Star Denotes a Sample Thermolyzed at 1100 °C without Further Annealing

	annealing temperature (°C)						
radiation	1100*	1200	1400	1600	1700	1850	2000
X-ray	3.36	3.72	4.19	5.30	5.92	8.22	9.62
neutrons	3.04	3.39	3.92	4.75	5.33	8.62	9.40

In summary, the present solid-state NMR study demonstrates that the B−C−N samples studied here consist of BN structures with mainly trigonally coordinated boron and nitrogen nuclei. So far, there is no evidence for the existence of B−C bonds, which again is in agreement with other precursor-derived ceramics.[41,46] At the same time, carbon exclusively exists as amorphous (graphite-like) carbon. Surprisingly, protons are detectable well beyond 1000 °C.

4.2. Inhomogeneities. 4.2.1. Small-Angle Scattering Cross Sections. Figure 8 shows the normalized SAS cross sections $I^N \equiv d\Sigma/d\Omega$ of amorphous ^{11}B−C−^{nat}N for X-rays and neutrons after annealing at different temperatures. It is obvious that there must be regions within the material which differ in atomic density and/or chemical composition from the surrounding matrix, giving rise to the observed signal.

For both experiments the SAS curves exhibit two regimes which are caused by different phenomena: Toward very small q values the scattered intensities show a linear increase in the log−log plot. This effect is caused by surface scattering from the powder particles according to Porod's law[16] and was subtracted in further data evaluation. At larger q values, a second scattering effect follows, which exhibits no distinct maximum, that is, no effect of interference. The type of scattering depends strongly on the annealing temperature. Increasing temperature causes an increase of intensity and also a shift of the observed signal toward lower q values. This clearly indicates that the size of the scattering regions p increases with increasing temperature. Furthermore, the curves show only a weak interference effect, which corresponds to a rather low volume fraction of the scattering regions within the sample.

4.2.2. Guinier Radii. If the signal is plotted as $\ln(I^N_{coh})$ versus q^2, the Guinier radius, R_G, can be determined from the slope of the linear part of this plot at small q values (cf. eq 8). Figure 9 shows the Guinier plot for X-ray and neutron scattering of the ^{11}B−C−^{nat}N ceramics annealed at different temperatures. The resulting Guinier radii are listed in Table 4. There is an increase of the radius from 3 Å in the as-thermolyzed condition up to about 9.5 Å after subsequent annealing for 16 h at 2000 °C. Therefore, from the Guinier investigations one can conclude that with increasing temperature the inhomogeneities within the samples are growing.

4.2.3. Modeling. In the following, a theoretical model for the description of the measured SAS data will be presented. For the determination of the intensity at zero scattering angle $I^N(q=0)$ the q range covered by the experiments had to be extended by an extrapolation procedure. Additionally, the weak observed interparticle interference and the surface scattering had to be taken into account. To solve these problems, the experimental data were fitted with a simple hard-sphere model.[16,18] For a system of hard spheres with radius R and a minimum distance $D > 2R$ the scattered intensity $I^N(q)$ can be worked out directly,

$$I^N(q) = I^N(0) \cdot F^2(q \cdot R) \left[1 - 8 \cdot n \frac{4\pi}{3}\left(\frac{D}{2}\right)^3 \cdot F(q \cdot D) \right] \quad (24)$$

where n is the number of spheres per volume:

$$F(q \cdot X) = \frac{3 \cdot (\sin(q \cdot X) - q \cdot X \cdot \cos(q \cdot X))}{(q \cdot X)^3}$$

It should be noted that the interparticle interference is overemphasized with the hard-sphere model because any other particle shape would allow closer packing of the particles. Therefore, the parameters n and D are not regarded as structural quantities but rather as variables to achieve a fit to the experimental data for the extrapolation of the q range. From the extrapolated curves the intensity at zero scattering angle $I^N(q=0)$ was determined. Figure 10 shows a fit of this model to the SANS data of ^{11}B−C−^{nat,15}N, annealed at 1600 °C for 16 h, including the Porod contribution at very small q values. In Table 5 the values for $I^N(q=0)$, R, D, and n, determined from the fits, are shown. The increase of the radius R with increasing temperature indicates that the structure shows coarsening, which confirms the above-mentioned Guinier investigations. Noting that the Guinier radius R_G of a spherical particle with radius R is $R_G = \sqrt{3/5}R$, a comparison of Tables 4 and 5 shows an accordance. Also, the value for the intensity at zero scattering angle $I^N(q=0)$ increases during further annealing. This fact will be considered in more detail later on.
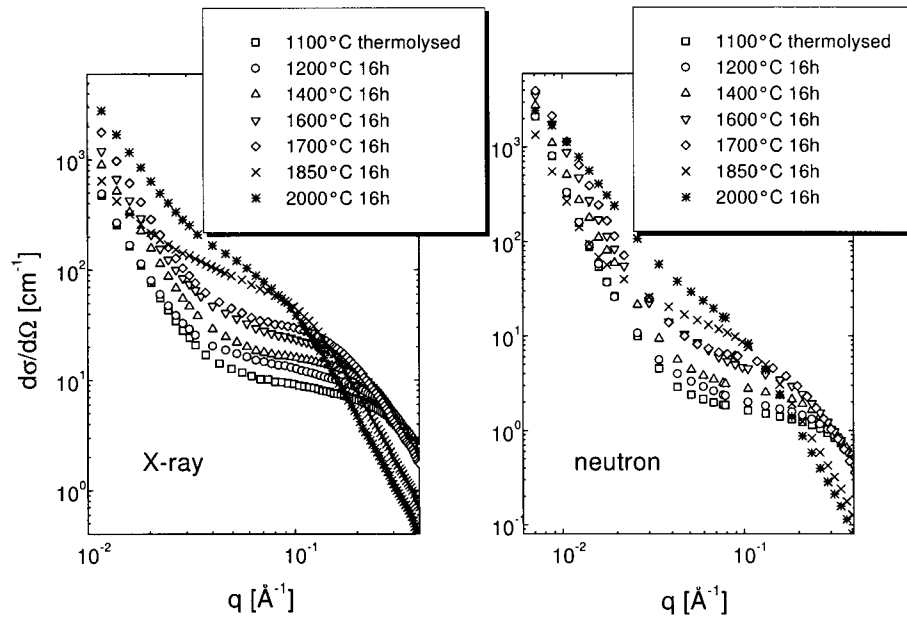
Figure 8. Small-angle scattering cross sections of amorphous ^{11}B−C−^{nat}N ceramics after annealing at different temperatures.

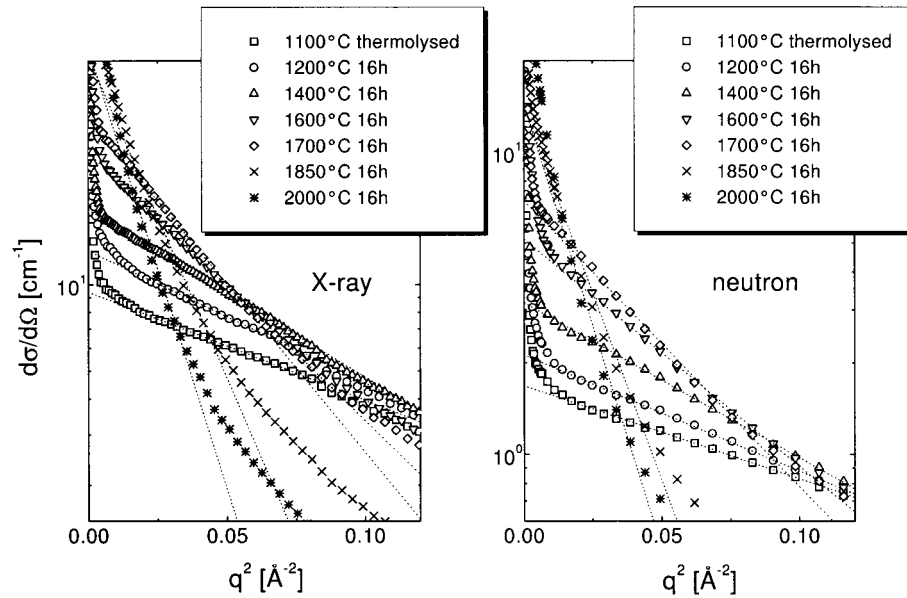**Figure 9.** Guinier plot of the SAS cross sections for the amorphous ^{11}B−C−^{nat}N ceramics after annealing at different temperatures.

Table 5. Parameters $\overline{\delta\eta^2}$, R, D, n, and $I^V(q{=}0)$ (See Text) Determined from Fits to the Experimental SAS Data Using a Hard-Sphere Model

sample parameter		radiation	coefficient				
structure formula	T (°C)	X-rays or neutrons	$\overline{\delta\eta^2}$ ($10^{-11} \cdot$ Å^{-4})	R (Å)	D (Å)	n ($10^{-6} \cdot$ Å^{-3})	$I^V(q{=}0)$ (cm^{-1})
^{11}B$_{35}$C$_{40}{}^{nat}$N$_{25}$	1100	X-rays	8.2	6.5	14.9	2.1	9.7
		neutrons	1.8	6.2	15.2	1.7	1.8
^{11}B$_{31}$C$_{39}{}^{nat}$N$_{30}$	1200	X-rays	8.7	7.2	15.5	1.2	13.6
		neutrons	1.8	6.9	14.9	1.4	2.4
^{11}B$_{34}$C$_{34}{}^{nat}$N$_{32}$	1400	X-rays	8.9	7.8	17.8	0.6	17.7
		neutrons	2.0	7.1	18.5	1.2	3.0
^{11}B$_{31}$C$_{37}{}^{nat}$N$_{32}$	1600	X-rays	7.2	9.7	25.5	0.5	27.9
		neutrons	1.8	9.1	22.0	0.8	5.5
^{11}B$_{32}$C$_{37}{}^{nat}$N$_{31}$	1700	X-rays	6.9	10.6	26.0	0.2	34.3
		neutrons	1.7	9.6	26.6	0.3	6.3
^{11}B$_{28}$C$_{44}{}^{nat}$N$_{14}{}^{15}$N$_{14}$	1600	X-rays	7.2	10.3	25.9	1.2	33.4
		neutrons	1.2	10.6	20.8	1.1	5.8

4.2.4. Identification of the Scattering Regions.

For the identification of the inhomogeneities, giving rise to a SAS effect, the contrast between the different scattering experiments is used. It is assumed that the B−C−N ceramics contain only one type of inhomogeneities, which differ in atomic density and/or chemical
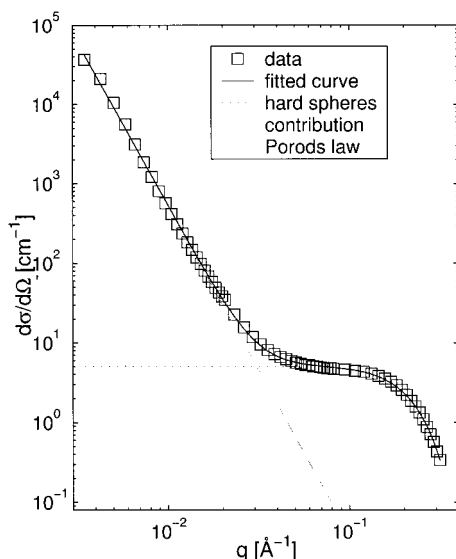
2868 *Chem. Mater., Vol. 14, No. 7, 2002*

Sauter et al.

Figure 10. Fit of hard-sphere model ($R = 10.6$ Å, $D = 20.8$ Å, $n = 1.1 \times 10^{-6}$ Å^{-3}, $I^N(q{=}0) = 5.8$ cm^{-1}) to the SANS data of ^{11}B$-$C$-^{nat,15}$N, annealed at 1600 °C for 16 h.

Table 6. Invariants Q^x and Q^n Determined from the Extrapolated SAS Data, for Neutron and X-ray Scattering

sample	T (°C)	Q^x (10^{24} cm^{-4})	Q^n (10^{24} cm^{-4})
^{11}B$_{35}$C$_{40}^{nat}$N$_{25}$	1100	222	34
^{11}B$_{31}$C$_{39}^{nat}$N$_{30}$	1200	256	42
^{11}B$_{34}$C$_{34}^{nat}$N$_{32}$	1400	270	47
^{11}B$_{31}$C$_{37}^{nat}$N$_{32}$	1600	249	53
^{11}B$_{32}$C$_{37}^{nat}$N$_{31}$	1700	233	43
^{11}B$_{28}$C$_{46}^{15}$N$_{13}^{nat}$N$_{13}$	1200	202	22
^{11}B$_{28}$C$_{44}^{15}$N$_{14}^{nat}$N$_{14}$	1600	234	31

composition from the surrounding matrix. Therefore, a two-phase model will be considered in the following.

First, the integrated intensity, the invariant Q, according to eq 9 was calculated. Therefore, the q range covered by the experiments had to be extended by an extrapolation procedure. By assuming that the intensity toward high q values obeys Porod's law (surface scattering from the regions) and after subtracting the intensity of surface scattering (from the powders particles) toward very small q values, the invariant Q was determined (q range: $0 < q < \infty$). In Table 6 the values for the invariants determined from the extrapolated data, for neutron as well as for X-ray scattering, are listed.

In the following a two-phase model for the inhomogeneities in B$-$C$-$N ceramics is proposed, which yields a quantitative description of the experimental SAS curves. In Table 7 relevant parameters, such as scattering lengths (b, f),[47] averaged scattering lengths densities $\langle\eta\rangle$, and microscopic densities ρ_0, are listed for the B$-$C$-$N ceramic matrix and for different phases which have to be considered as conceivable scattering regions. The microscopic densities for the regions were determined from the densities of commercial crystalline products and in the case of BC$_2$N and BC$_4$N by reasonable estimations. The contrast between possible regions

(47) Koester, L.; Yelon, W. B. Summary of low energy neutron scattering lengths and cross-sections. In *Theory of Neutron Scattering from Condensed Matter*; Lovesey, S. W., Ed.; International Series of Monographs on Physics, 72; Clarendon Press: Oxford, 1984; Vol. 1 (Nuclear scattering).
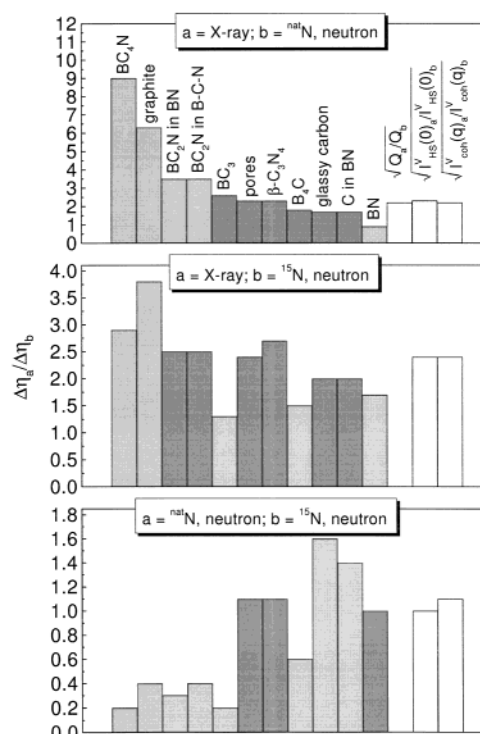

Figure 11. The three different experimental ratios, given by the white-colored bars on the right, were calculated by using the invariant Q, the coherent scattered intensity $I(q{=}0)$ derived from the model, and the coherent scattered intensity $I(q)$ (q range: $0.05 < q < 0.1$), respectively. These ratios, derived from the SANS and SAXS experiments, are compared with the values $\Delta\eta_a/\Delta\eta_b$, as expected for different types of possible region$-$matrix combinations, which are given by the colored bars (black and gray) on the left. Those calculated bars for the expected possible region$-$matrix combinations, which show the best agreement with the experimental bars, are highlighted in black.

and the B$-$C$-$N matrix annealed at 1600 °C, that is, the squared difference $(\Delta\eta)^2$ between the scattering length densities, is listed in Table 8 as a measure for the visibility of a certain type of regions in the SAS experiments. It should be noted that the regions, of whatever type, are still amorphous because wide-angle scattering did not indicate any traces of crystalline peaks up to 1600 °C.

For the sake of completeness in the following discussion of different scattering regions, the material will also be considered as a two-phase system, consisting either of amorphous BC$_2$N and amorphous boron nitride or of amorphous carbon and amorphous boron nitride, which are dispersed in each other. This is obvious because the chemical composition of the sample can be subdivided in a formal way into these two phases.

The values for $(\Delta\eta)^2$ in Table 8 are given for the case of a small volume fraction of the segregated phase, that is, for a negligible change of the chemical composition of the B$-$C$-$N matrix. Note that in the case of a substantial amount of a segregated phase the scattering length density of the remaining matrix may change considerably, causing an increase of the contrast between the precipitates and the matrix (see, e.g., ref 48).

(48) Schempp, S.; Dürr, J.; Lamparter, P.; Bill, J.; Aldinger, F. *Z. Naturforschung* **1998**, *53a*, 127$-$133.

Table 7. Microscopic Densities ρ_0, Average Scattering Lengths $\langle b \rangle$, and Scattering Length Densities η of B−C−N Ceramics (Annealed at 1600 °C) and Possible Regions

		neutrons		X-rays	
phase	density ρ_0 (1/Å³)	$\langle b \rangle$ (10^{-12} cm)	η^n (10^{10} cm^{-2})	$\langle b \rangle$ (10^{-12} cm)	η^x (10^{10} cm^{-2})
^{11}B−C−^{nat}N	0.104	0.75	7.80	1.69	17.58
^{11}B−C−^{nat,15}N	0.098	0.70	6.85	1.69	16.50
GC	0.077[a]	0.665	5.119	1.686	12.985
graphite	0.114[59,53]	0.665	7.552	1.686	19.158
^{11}B$_4$C	0.136[60]	0.666	9.022	1.462	19.805
^{11}B^{nat}N	0.109[53,61,62]	0.798	8.722	1.686	18.432
^{11}B^{15,nat}N	0.107[53,61,62]	0.727	7.788	1.686	18.078
β-C$_3$^{nat}N$_4$	0.160[63,64]	0.816	12.970	1.847	29.515
β-C$_3$^{15,nat}N$_4$	0.157[63,64]	0.735	11.497	1.847	28.906
^{11}BC$_2$^{nat}N	0.111[b]	0.731	8.148	1.686	18.787
^{11}BC$_2$^{15,nat}N	0.110[b]	0.696	7.674	1.686	18.601
^{11}BC$_4$^{nat}N	0.112[b]	0.709	7.950	1.686	18.905
^{11}BC$_4$^{15,nat}N	0.111[b]	0.685	7.635	1.686	18.787
^{11}BC$_3$	0.113[65]	0.665	7.529	1.616	18.295

[a] Derived from measurements. [b] Derived by reasonable estimations.

Table 8. Calculated Contrast ($\Delta\eta$) between Conceivable Regions and the B−C−N Matrix; In Addition, the Values for the Two-Phase Models of BC$_2$N in Boron Nitride and Glassy Carbon in Boron Nitride Are Given

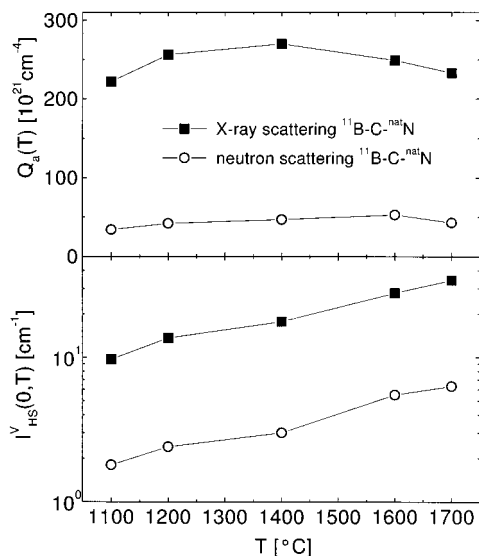| sample	contrast (10^{10} cm^{-2})	region−matrix (B−C−N) combinations									BC$_2$N BN	C BN
		C	GC	pores	B$_4$C	BN	β-C$_3$N$_4$	BC$_2$N	BC$_4$N	BC$_3$		
^{11}B−C−^{nat}N	$\Delta\eta^x$	1.58	4.59	17.58	2.23	0.86	11.94	1.21	1.33	0.72	3.94	9.2
1600 °C	$\Delta\eta^n$	0.25	2.69	7.80	1.22	0.92	5.17	0.34	0.15	0.28	1.12	5.4
^{11}B−C−^{nat,15}N	$\Delta\eta^x$	2.66	3.51	16.50	3.31	1.58	12.41	2.10	2.29	1.80	9.57	8.1
1600 °C	$\Delta\eta^n$	0.71	1.73	6.85	2.18	0.94	4.65	0.83	0.79	1.37	3.78	4.0

Figure 12. (a) Invariant Q and (b) $I^V(q=0)$, determined from the extrapolated experimental data as a function of the annealing temperature.

Figure 11 shows the results of the contrast variation for B−C−N annealed at 1600 °C. The three different experimental ratios were calculated by using the invariant Q, the coherent scattered intensity $I(q=0)$ derived from the model, and the coherent scattered intensity $I(q)$ (q range: $0.05 < q < 0.1$), respectively. These ratios, $\Delta\eta^a/\Delta\eta^b$, derived according to eq 13 from the SANS and SAXS experiments are compared with the values as expected for different types of inhomogeneities. Also, the expected values for the two-phase systems BC$_2$N/BN and C/BN are listed. In a comparison of the ratios derived from the experiments with the expected values for different inhomogeneities and the two-phase systems, respectively, it can be seen that two possibilities show the best agreement with the experimental data:

C$_3$N$_4$ or submicroscopic pores, dispersed in an amorphous B−C−N matrix.

In the case of C$_3$N$_4$ heterogeneities one would expect an increase of the volume fraction with time and temperature upon annealing. If the system tends to form a C$_3$N$_4$ phase in a B−C−N matrix, there is no reason conceivable that this process does not proceed further during annealing. This would be associated with an increase of the invariant Q. However, this was not observed as one can see in Figure 12a. The invariant Q remained nearly constant over the whole applied temperature range; that is, the volume fraction c of the heterogeneities and the difference of the scattering length densities $(\Delta\eta)^2$ remain constant, too. The reason for the increase of the observed SAS signal with increasing temperature is the increase of the correlation volume V_c, that is, the intensity at zero scattering angle $I^V(q=0)$ increases as shown in Figure 12b.

The observation that the invariant Q remains constant during annealing can be understood if it is assumed that the heterogeneities are of the second type: submicroscopic pores in a B−C−N matrix that consists of a substitutional solid solution of all three elements in a honeycomb network. The atomic density of the matrix, the contrast $\Delta\eta$, and the volume fraction of the pores do not change by annealing, too. Therefore, the increase of the radius of the pores with increasing temperature indicates that coarsening of the pores is taking place, which can be conceived as Ostwald-ripening of the free volume, driven by the reduction of pore surface. The volume fraction of the pores was determined from Q according to eq 9 to be $\approx$4 vol %. Positron annihilation experiments revealed[49] also that

(49) Schaefer, H.-E. personal communication, 1999.
(50) Hom, T.; Kiszenick, W.; Post, B. *J. Appl. Crystallogr.* **1975**, *8*, 457−458.
(51) Sung, C.-M.; Sung, M. *Mater. Chem. Phys.* **1996**, *43*, 1−18.
(52) Trucano, P.; Chen, R. *Nature* **1975**, *258*, 136−137.

the as-prepared amorphous B−C−N ceramics contain regions of free volume with an average size of about 6 Å, which is in accordance with the results obtained from SAS.

It should be noted that the above discussion was based on the assumption of one type of inhomogeneities only in a matrix. It cannot be excluded that more types of inhomogeneities are present in the real material, for example, a preference of B−N and C−C bonding in the amorphous structure.

5. Conclusions

B−C−N ceramics derived from $[B_2(NCN)_3]_n$ predominantly contain 3-fold-coordinated boron, carbon, and nitrogen atoms in hexagonal planar arrangements. The atomic distances are similar to the corresponding distances in hexagonal boron nitride and graphite, respectively.

Small-angle scattering experiments revealed that the amorphous B−C−N ceramics consist of a BCN phase and voids in the medium-range order. NMR, which is more sensitive to short-range order phenomena, shows the presence of BN structures with mainly trigonally coordinated boron and nitrogen nuclei and the presence of amorphous (graphite-like) carbon within the B−C−N ceramics at the same time. This indicates that the BCN phase is separated in BN and C phases. This means that the investigated BCN ceramics show short-range phase separation into BN and C regions.

Additionally, in the as-prepared state the material contains nanopores with sizes on the order of about 10 Å. During annealing the size of the pores increases with increasing temperature; however, the volume fraction remains nearly constant. This coarsening can be conceived as Ostwald ripening of the pores.

CM011081G

(53) Greenwood, N. N.; Earnshaw, E. *Chemie der Elemente*; VCH: Weinheim, 1990.

(54) Robertson, J. *Adv. Phys.* **1986**, *35* (4), 317−374.

(55) Pease, R. S. *Acta Crystallogr.* **1952**, *5*, 356−361.

(56) Fukunaga, T.; Goto, T.; Misawa, M.; Hirai, T.; Suzuki, K. *J. Non-Cryst. Solids* **1987**, *95/96*, 1119−1125.

(57) Tománek, D.; Wentzcovitch, R. M.; Louie, S. G.; Cohen, M. L. *Phys. Rev. B* **1988**, *37* (6), 3134−3137.

(58) Hughbanks, T.; Tian, Y. *Solid State Commun.* **1995**, *96*, 321−325.

(59) v. Sturm, F. *Nachr. Chem. Techn. Lab.* **1987**, *35* (9).

(60) Clark, H. K.; Hoard, J. L. *J. Am. Chem. Soc.* **1943**, *65*, 2115−2119.

(61) Lipp, A.; Schwetz, K. A.; Hunold, K. *J. Eur. Ceram. Soc.* **1989**, *5*, 3−9.

(62) Paine, R. T.; Narula, C. K. *Chem. Rev.* **1990**, *90*, 73−91.

(63) Cohen, M. L. *J. Hard. Mater.* **1991**, *2* (1−2), 13−27.

(64) Riedel, R. *Adv. Mater.* **1994**, *6* (7/8), 549−560.

(65) Kouvetakis, J.; Kaner, R. B.; Sattler, M. L.; Bartlett, N. *J. Chem. Soc., Chem. Commun.* **1986**, 1758−1759.